Supplementary Information for

Spontaneous Enhancement of Dzyaloshinskii-Moriya Interaction via Field-Cooling-Induced Interface Engineering in 2D Ferromagnetic ternary Tellurides

Shian Xia[1, #], Yan Luo[2, #], Iftikhar Ahmed Malik[1, #], Xinyi Zhou[1], Keying Han[3], Yue Sun[1], Haoyun Lin[1], Hanqing Shi[4], Xiaoze Liu[1], Yingchun Cheng[3], Vanessa Li Zhang[1], Yi Du[4], Sheng Liu[1,5*], Chao Zhu[2*], Ting Yu[1,6,7*]

[1]School of Physics and Technology, Wuhan University, Wuchang District, Hubei 430072, China.

[2]SEU-FEI Nano-Pico Center, Key Lab of MEMS of Ministry of Education, School of Integrated Circuits, Southeast University, Nanjing 210096, China.

[3]Hebei Key Laboratory of Microstructure Materials Physics, School of Science, Yanshan University, Qinhuangdao, 066004, China.

[4]School of Physics, Beihang University, Haidian District, Beijing 100191, China.

[5]Wuhan National High Magnetic Field Center, Huazhong University of Science & Technology, Wuhan 430074, China.

[6]Wuhan Institute of Quantum Technology, Wuhan 430206, China.

[7]Key Laboratory of Artificial Micro- and Nano- structures of Ministry of Education, Wuhan University, Wuhan 430072, China.

# These authors contributed equally to this work.

* Correspondence to E-mail: yu.ting@whu.edu.cn; phczhu@seu.edu.cn; liu.sheng@whu.edu.cn

Table of Contents

Supplementary Figures

Figure S18. HAADF-STEM images of the edge of pristine FGeT.

Figure S19. ADF-STEM image of large-scale $FeTe_2$ after annealed FGeT

Figure S20. Field-dependent magnetic force microscopy (MFM) imaging of pristine FGeT.

Figure S21. Field-dependent magnetic force microscopy (MFM) imaging of annealed FGeT.

Figure S22. Thickness and temperature dependence of Raman spectra in FGaT

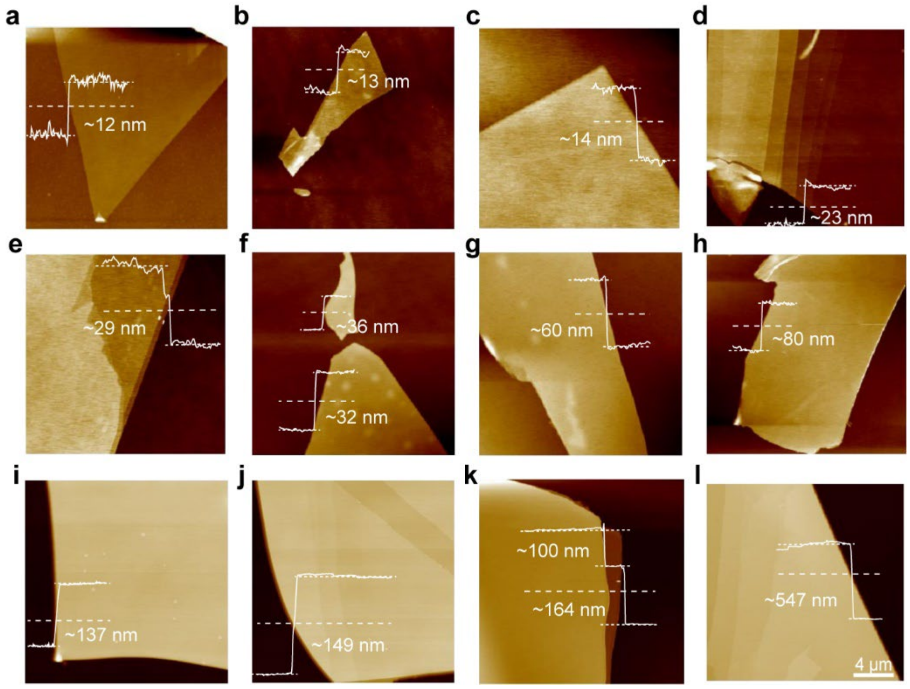

Figure S1 | Atomic force microscopy (AFM) characterization of FGaT flakes with varying thicknesses. Atomic force microscopy (AFM) images of FGaT flakes with varying thicknesses. **(a–l)** AFM topography scans of exfoliated FGaT flakes, illustrating thickness measurements ranging from ~12 nm to ~547 nm, as determined via step height analysis. White dashed lines denote the locations of the height profiles, with corresponding step height plots provided in each panel. The scale bar is 4

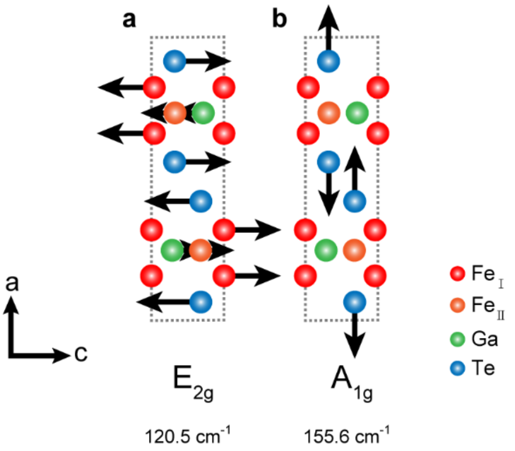

Figure S2 | Calculated atomic displacement patterns of Raman-active modes in bulk FGaT. (a) E_{2g} mode at 120.5 cm^{-1}, corresponding to the in-plane vibrational motion of Fe, Ga, and Te atoms. **(b)** A_{1g} mode at 155.6 cm^{-1}, representing out-of-plane vibrations. Black arrows denote the direction of atomic displacements. These vibrational modes serve as characteristic signatures of FGaT, providing key insights into lattice dynamics and phase transformations.

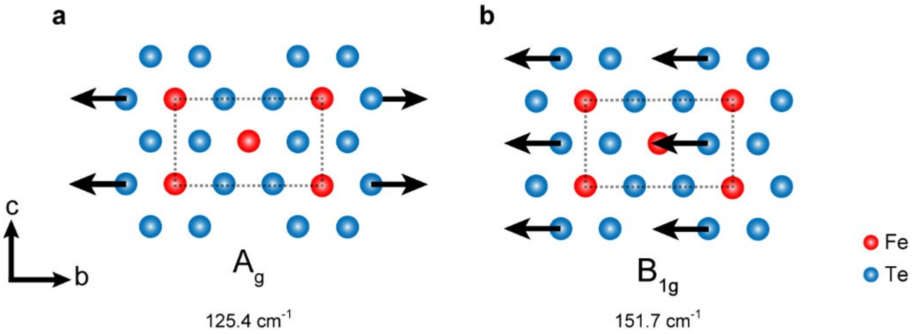

Figure S3 | Calculated atomic displacement patterns of Raman-active modes in bulk orthogonal FeTe$_2$. (a) A$_g$ mode at 125.4 cm^{-1}, corresponding to symmetric in-plane vibrations of Fe and Te atoms. **(b)** B$_{1g}$ mode at 151.7 cm^{-1}, associated with asymmetric atomic displacements. Black arrows denote the direction of atomic motion. These vibrational modes serve as characteristic signatures of FeTe$_2$, offering insight into its lattice dynamics and structural properties.

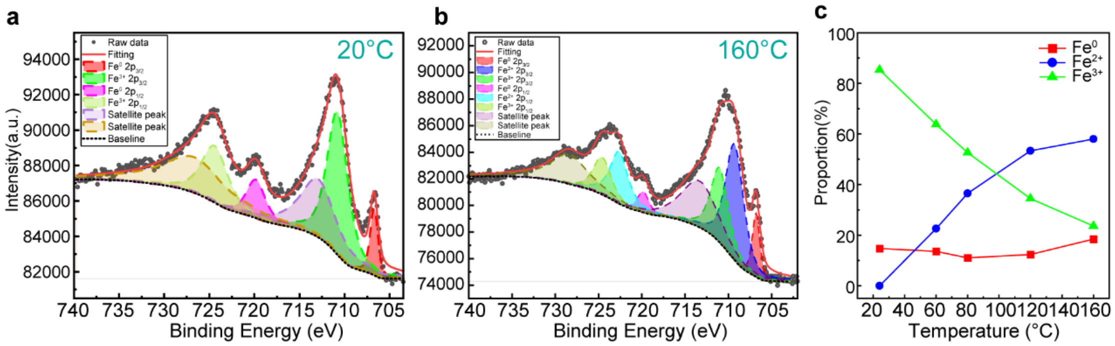

Figure S4 | X-ray photoelectron spectroscopy (XPS) analysis of the exfoliated fresh FGaT crystal surface. (a, b) High-resolution Fe 2p spectra recorded at 20 °C **(a)** and 160 °C **(b)**, illustrating the evolution of Fe valance states. Spectral deconvolution reveals contributions from Fe^0, Fe^{2+}, and Fe^{3+}, indicating temperature-induced modifications in the chemical environment. **(c)** Temperature-dependent evolution of Fe valence states, showing a progressive increase in Fe^{2+} content with temperature, consistent with $FeTe_2$ precipitation, while Fe^{3+} concentration decreases. These findings support the temperature-driven transformation of FGaT and the emergence of $FeTe_2$.

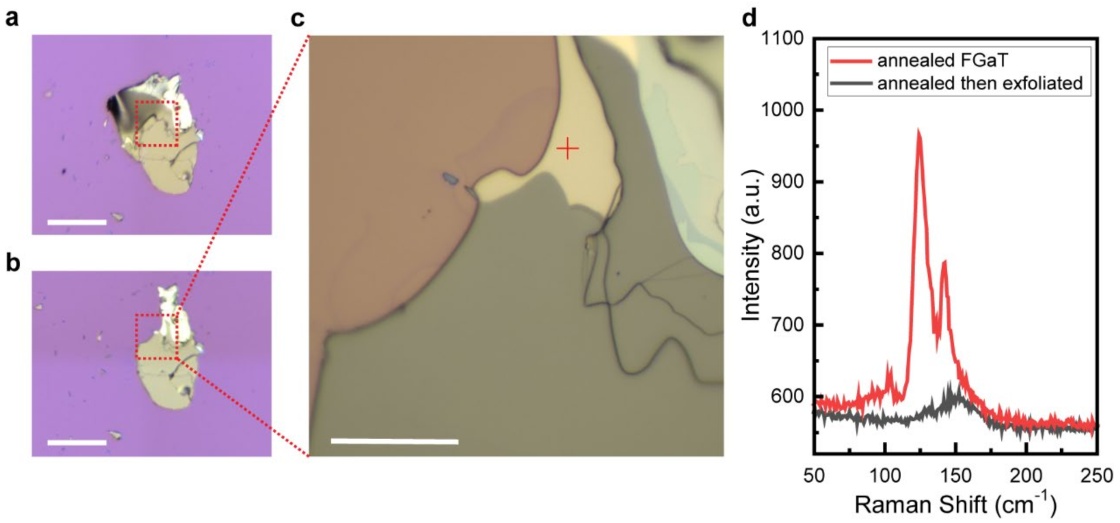

Figure S5 | Raman analysis of re-exfoliated annealed FGaT (a) Optical image of annealed FGaT prior to exfoliation. **(b, c)** Optical images of FGaT after re-exfoliation, revealing the exposed inner layers. **(d)** Raman spectra comparison between annealed FGaT (red) and the re-exfoliated layer (black). The re-exfoliated sample displays only the characteristic peaks of FGaT, while $FeTe_2$-related peaks are absent, confirming that $FeTe_2$ precipitates predominantly on the surface following annealing. Scale bars: 100 μm **(a, b)**, 20 μm **(c)**.

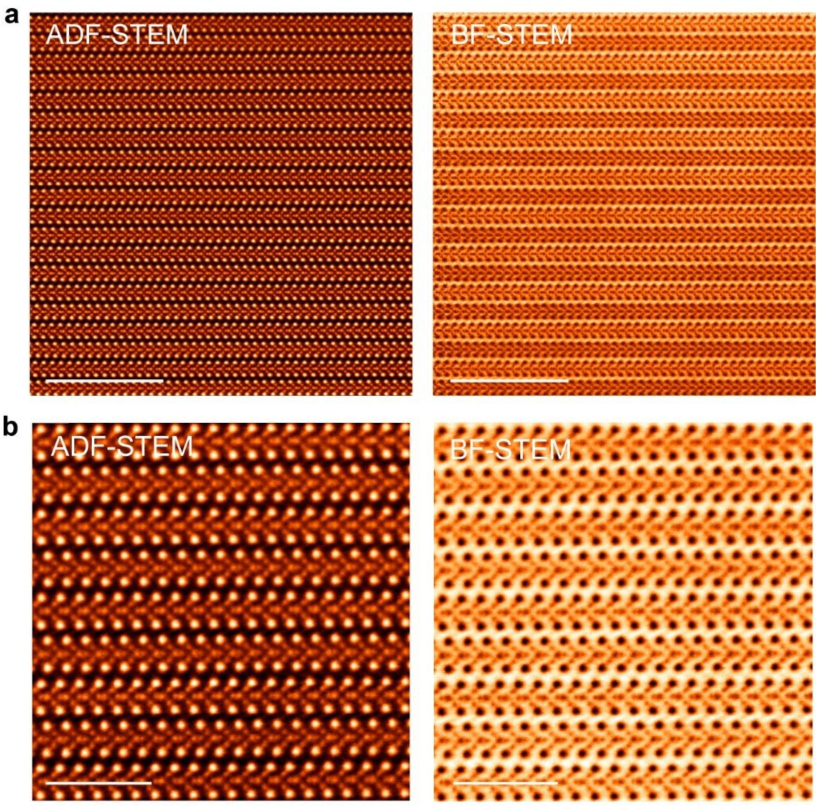

Figure S6 |The atomic structure of pristine FGaT. (a, b) Annular dark field **(**ADF)-STEM images (left panel) and corresponding BF (bright field)-STEM images (right panel) of pristine FGaT taken along [1 0 0] zone axis. Scale bars: 2 nm in **(a)**; 5 nm in **(b)**.

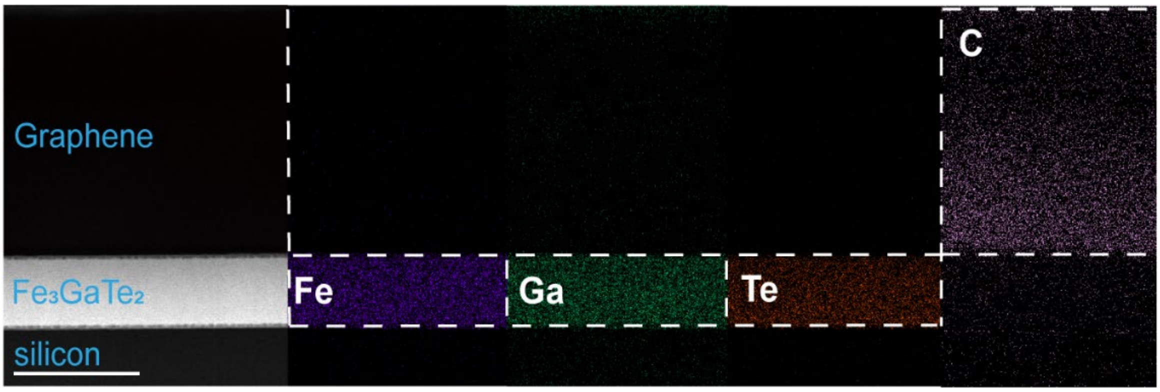

Figure S7 | Corres-sectional ADF-STEM image of Graphene capped-FGaT and corresponding Energy dispersive X-ray spectroscopy (EDS) mapping.

STEM image of the FGaT with a graphene capping layer and corresponding EDS elemental mapping. The EDS maps confirm the spatial distribution of Fe (purple), Ga (green), Te (orange), and C (pink), illustrating the composition of the FGaT layer, graphene capping, and underlying silicon substrate. Scale bars: 200 nm**.**

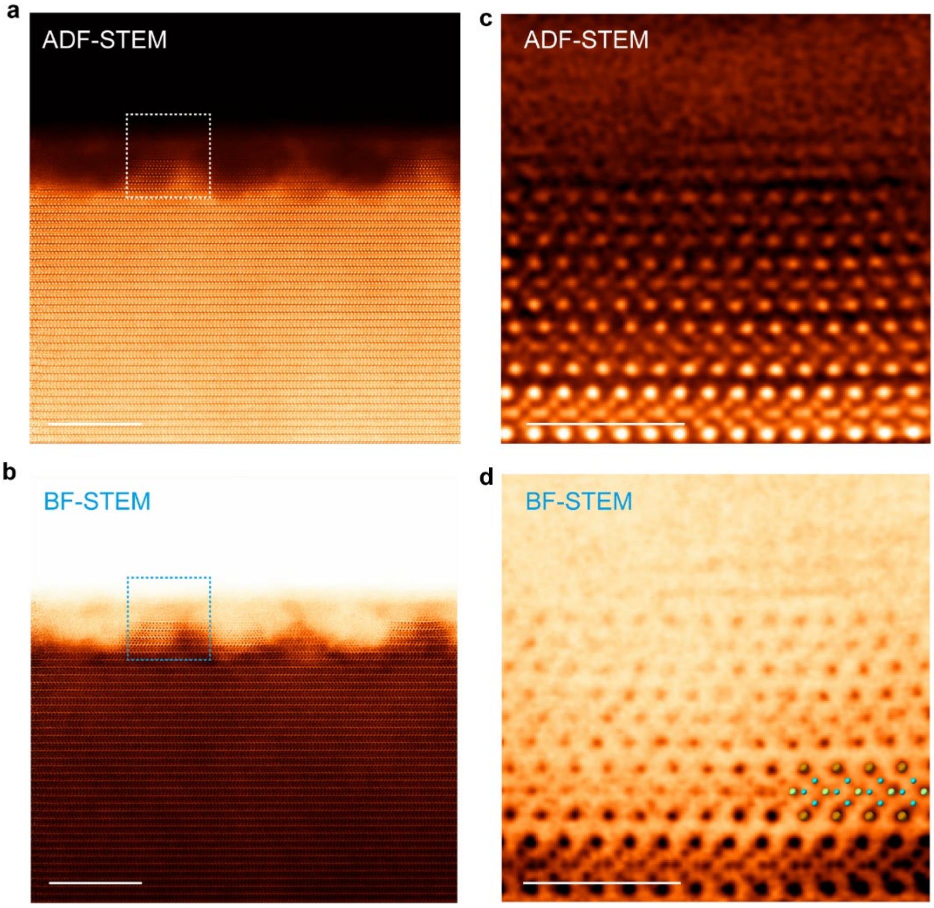

Figure S8 | HAADF-STEM images of the edge of pristine FGaT. (a) ADF-STEM image and **(b)** corresponding BF-STEM image showing the edge of pristine FGaT. **(c, d)** zoomed in STEM images of the dotted squares from **a** and **b** respectively. The color balls in **(d)** represent Fe (blue), Te (orange), and Ga (green) atoms, respectively. Scale bars: 10 nm in **(a)** and **(b)**; 2 nm in **(c)** and **(d)**.

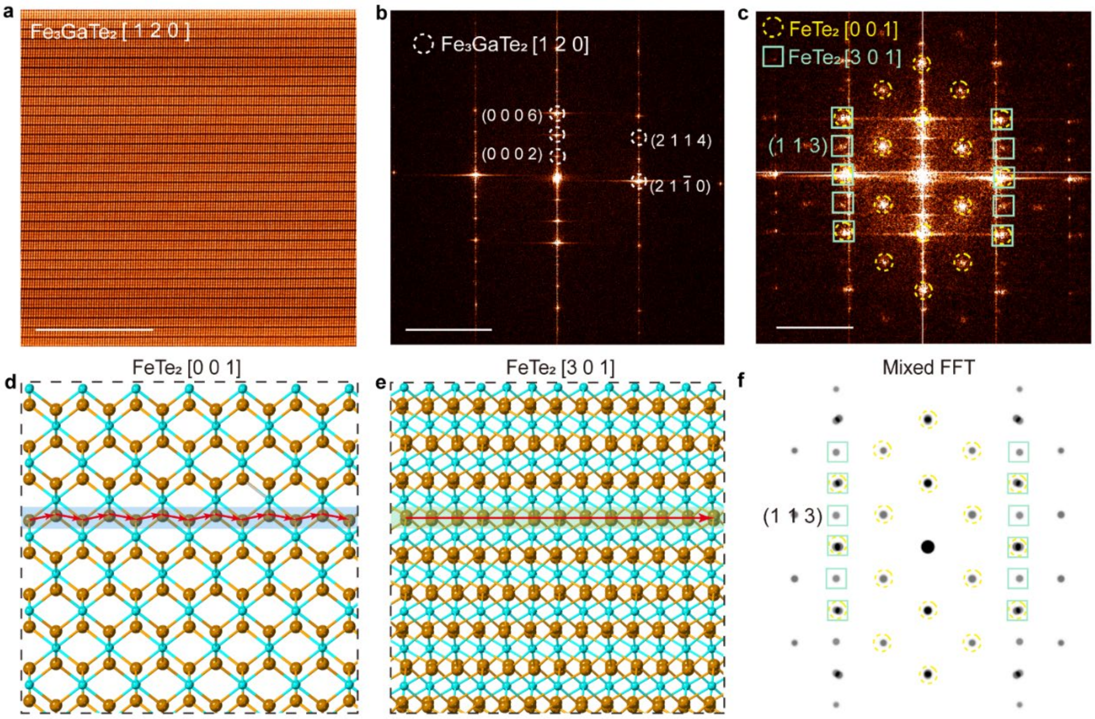

Figure S9 | Atomic structure of FeTe$_2$ formed along the [1 2 0] direction in annealed FGaT. **(a)** ADF-STEM image of pristine FGaT along the [1 2 0] zone axis. **(b)** Corresponding fast Fourier transform (FFT) image of pristine FGaT, showing its characteristic diffraction spots. **(c)** FFT pattern of annealed FGaT from Figure 2e, highlighting diffraction spots associated with FeTe$_2$ [0 0 1] (yellow circles) and FeTe$_2$ [3 0 1] (green squares), confirming the coexistence of FeTe$_2$ in multiple orientations. **(d, e)** Atomic models of FeTe$_2$ viewed along the [0 0 1] and [3 0 1] zone axes, respectively, illustrating structural variations, with red arrows indicating Te atomic displacement differences between the two orientations. **(f)** Simulated mixed FFT pattern incorporating FeTe$_2$ [0 0 1] and [3 0 1] diffraction spots, demonstrating excellent agreement with the experimental FFT pattern in **(c)**. Scale bars: 10 nm in **(a)** and **(d)**; 5 nm^{-1} in **(b)** and **(c)**.

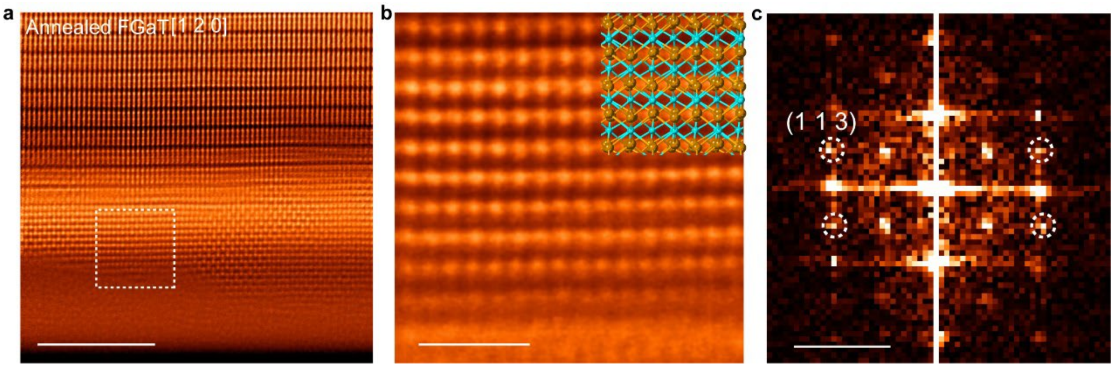

Figure S10 | The formation of [3 0 1] FeTe$_2$ along the [1 2 0] direction of annealed FGaT. (a) Large scale ADF-STEM image of annealed FGaT along the [1 2 0] zone axis. **(b)** High-resolution ADF-STEM image stacking of [0 0 1] and [3 0 1] FeTe$_2$, derived from white dashed square **(a)**. **(c)** Corresponding FFT image showing characteristic (1 1 3) diffraction spots. The observed spots from [0 0 1] FeTe$_2$ are likely attributed to the stacking of [0 0 1] and [3 0 1] FeTe$_2$. Scale bars: 5 nm in **a**; 1 nm in **b**; 5 nm^{-1} in **c.**

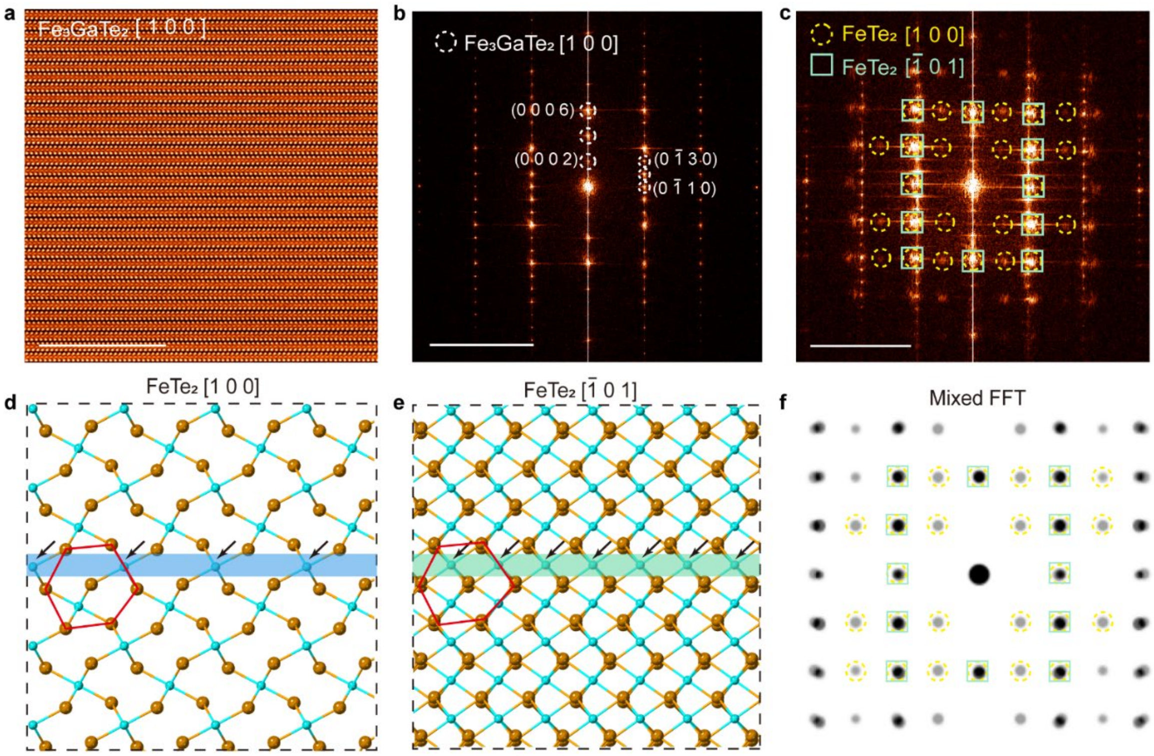

Figure S11 | Atomic structure of $FeTe_2$ formed along the [1 0 0] direction in annealed FGaT. **(a)** ADF-STEM image of pristine FGaT taken along [1 0 0] zone axis and **(b)** Corresponding fast Fourier transform (FFT) image of pristine FGaT, showing its characteristic diffraction spots. **(c)** FFT pattern of annealed FGaT from Figure 2f, highlighting diffraction spots associated with $FeTe_2$ [1 0 0] (yellow circles) and $FeTe_2$ [$\bar{1}$ 0 1] (green squares), confirming the coexistence of $FeTe_2$ in multiple orientations. **(d, e)** Atomic models of $FeTe_2$ viewed along the [1 0 0] and [$\bar{1}$ 0 1] zone axes, respectively, illustrating structural variations, with red arrows indicating Te atomic displacement differences between the two orientations. **(f)** Simulated mixed FFT pattern incorporating $FeTe_2$ [1 0 0] and [$\bar{1}$ 0 1] diffraction spots, demonstrating excellent agreement with the experimental FFT pattern in **(c)**. Scale bars: 10 nm in **a**, **d**; 5 nm^{-1} in **b** and **c**.

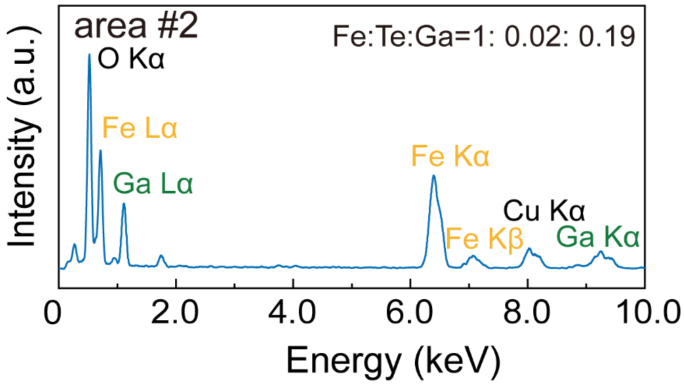

Figure S12 | EDS spectrum of Area #2 from Fig. 2l, revealing the elemental composition of the FGaT layer above the $FeTe_2$ region.

EDS spectrum of Area #2 from Fig. 2l, showing the elemental distribution within the FGaT layer above the $FeTe_2$ region. The measured Fe: Te: Ga ratio of 1: 0.02: 0.19 indicates significant Te depletion, suggesting that this region consists primarily of Fe rather than $FeTe_2$. These findings indicate that Area #2 corresponds to an Fe-rich phase, potentially amorphous or disordered Fe, resulting from the excess Fe during annealing.

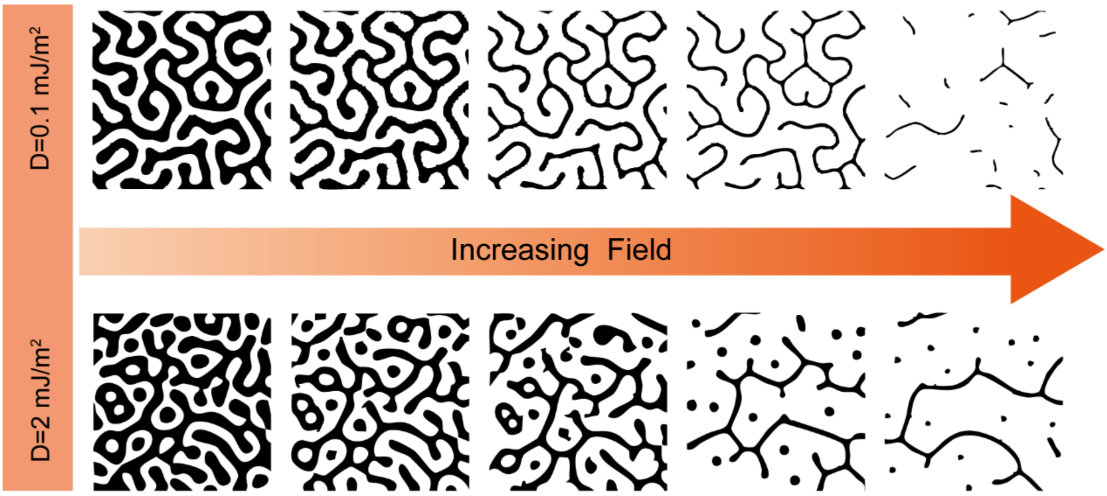

Figure S13 | Micromagnetic simulation results on evolution of spin textures under external magnetic field in prinstine FGaT and FeTe$_2$/FGaT interface.

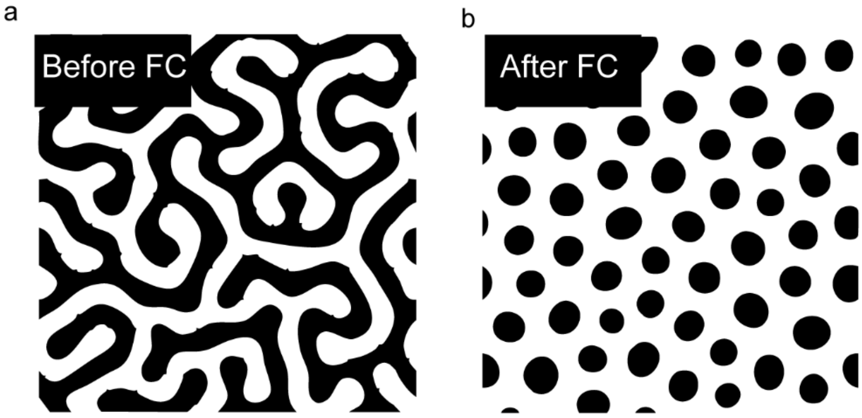

Figure S14 | Simulated generation of skyrmion lattices after FC in $FeTe_2$/FGaT interface.

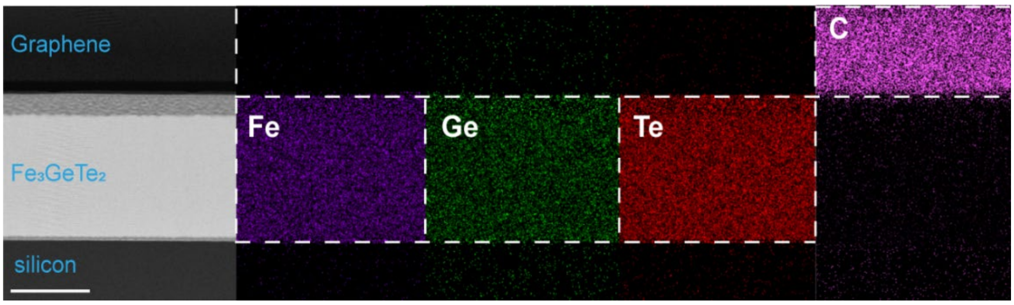

Figure S15 | Corres-sectional ADF-STEM image of Graphene capped-FGeT and corresponding Energy dispersive X-ray spectroscopy (EDS) mapping.

STEM image of the FGeT with a graphene capping layer and corresponding EDS elemental mapping. The EDS maps confirm the spatial distribution of Fe (purple), Ge (green), Te (orange), and C (pink), illustrating the composition of the FGeT layer, graphene capping, and underlying silicon substrate. Scale bars: 200 nm**.**

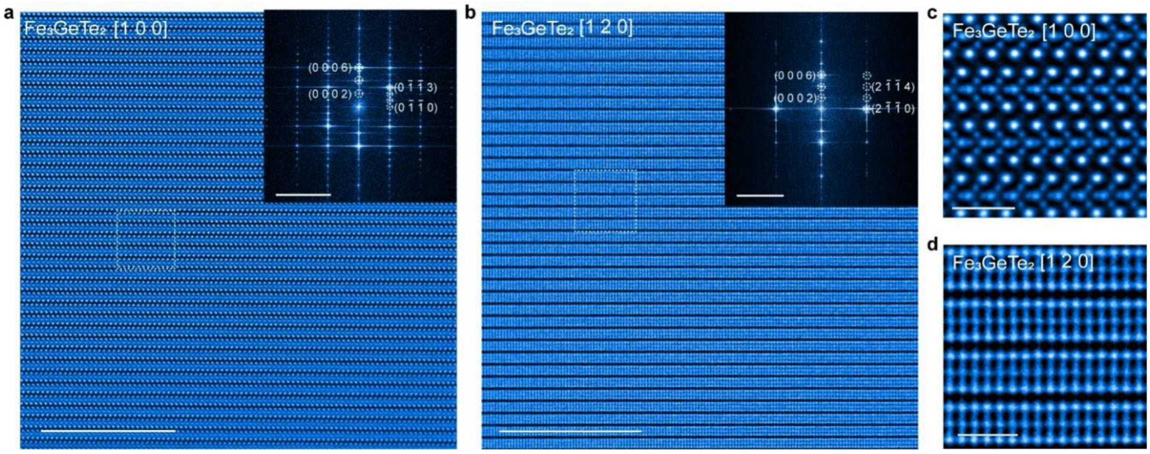

Figure S16 | HAADF-STEM images of atomic structure of pristine FGeT. (a, b) ADF-STEM images of pristine FGeT viewed along [1 0 0] and [1 2 0] zone axes, respectively. Insets display the corresponding FFT patterns, confirming the crystallographic orientation. **(c, d)** High-resolution ADF-STEM images of white dashed squares in **(a)** and **(b)**, respectively, showing detailed atomic arrangements. Scale bars: 10 nm in **(a)** and **(b)**; 5 nm^{-1} in inset of **(a)** and **(b)**; 1 nm in **(c)** and **(d)**.

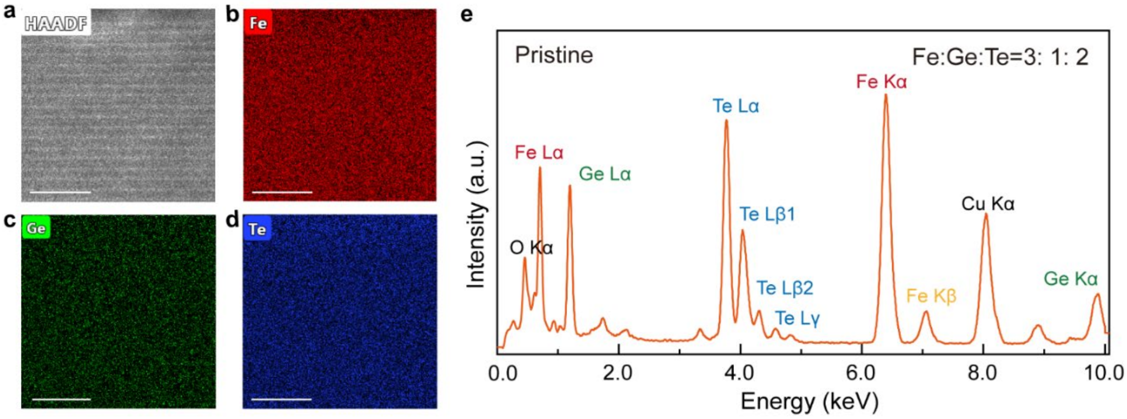

Figure S17 | The EDS mapping and spectrum of pristine FGeT. (a) Cross-sectional STEM images of pristine FGeT, along with corresponding EDS elemental mappings for **(b)** Fe, **(c)** Ge and **(d)** Te elements. **(e)** Quantitative analysis of EDS revealing the ratios of Fe: Ge: Te is 3: 2: 1. Scale bars: 5 nm.

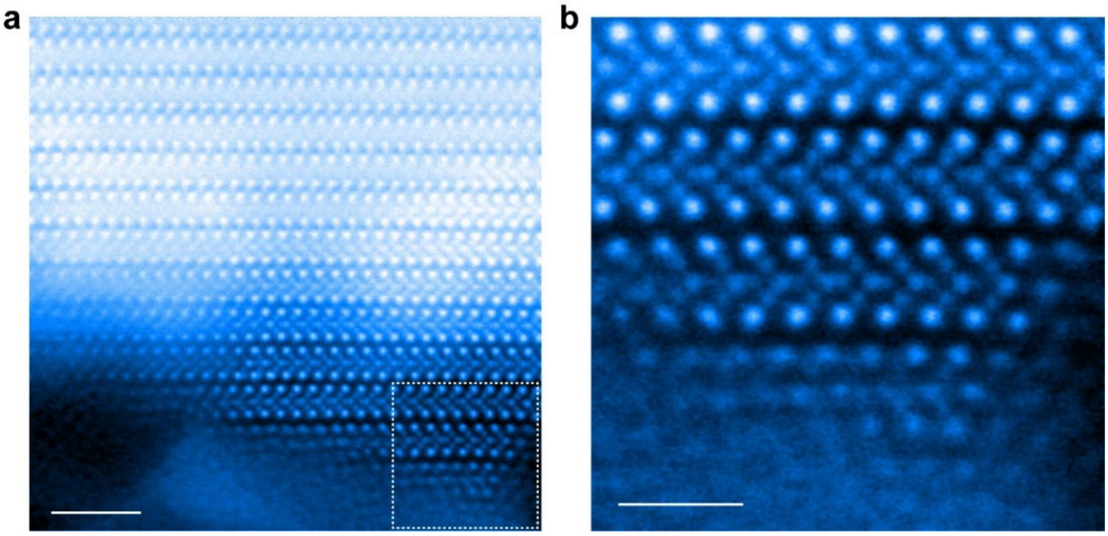

Figure S18 | HAADF-STEM images of the edge of pristine FGeT. (a) ADF-STEM image showing the edge of pristine FGeT. **(b)** zoomed in STEM images of the dotted squares from **(a)**. Scale bars: 10 nm in **(a)** and **(b)**; 2 nm in **(c)** and **(d)**.

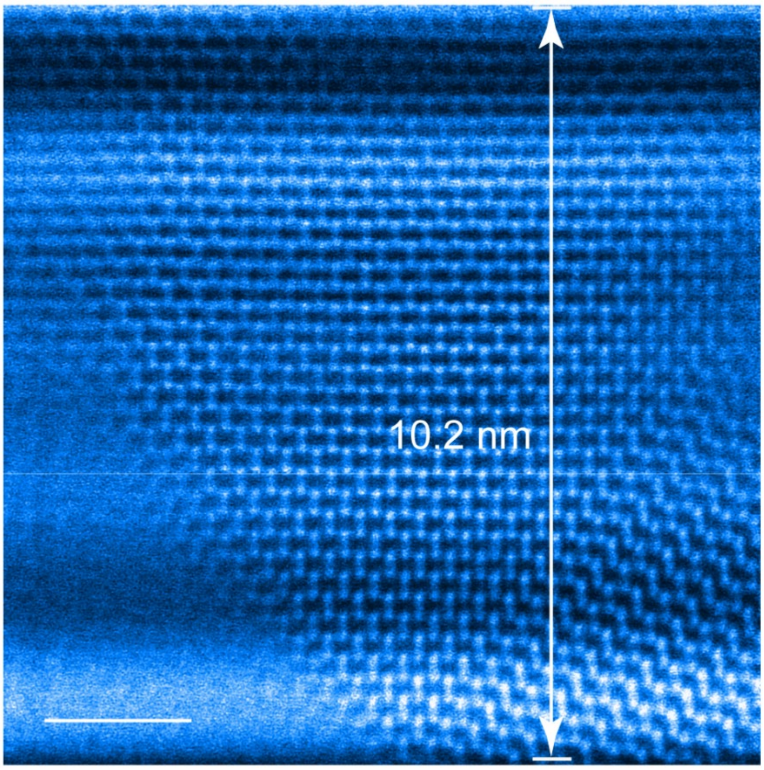

Figure S19 | ADF-STEM image of large-scale $FeTe_2$ after annealed FGeT. Scale bar: 2 nm.

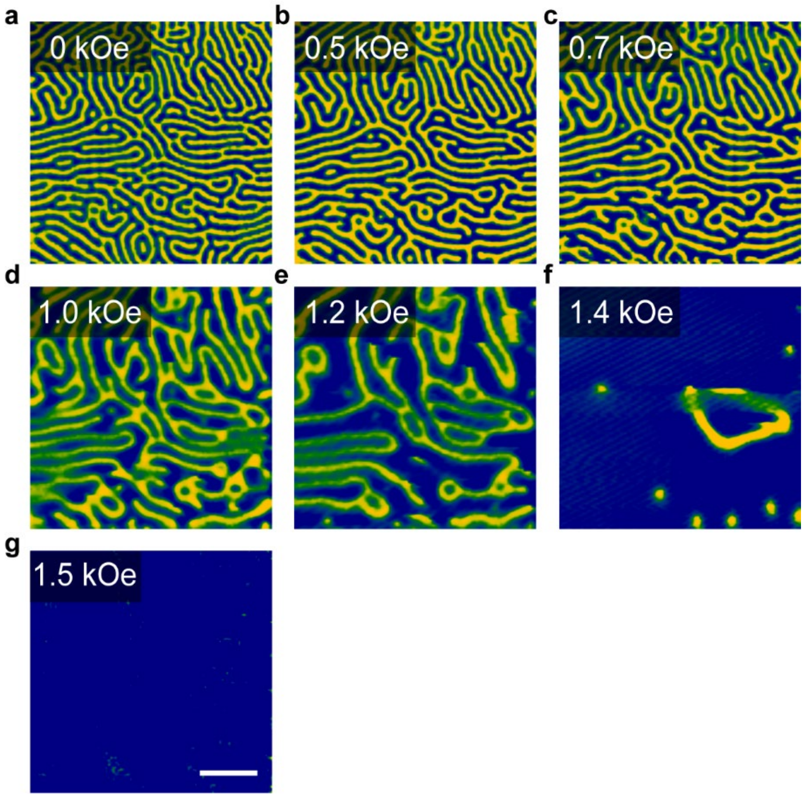

Figure S20 | Field-dependent magnetic force microscopy (MFM) imaging of pristine FGeT. (a–g) MFM images obtained under increasing external magnetic fields from 0 kOe to 1.5 kOe, illustrating the evolution of magnetic domain structures. At 0 kOe **(a)**, a well-defined labyrinth-like domain pattern is observed. As the field increases to 0.5 kOe **(b)** and 0.7 kOe **(c)**, the labyrinthine structure remains stable. At 1.0 kOe **(d)** and 1.2 kOe **(e)**, domains begin to fragment, giving rise to isolated skyrmions. At 1.4 kOe **(f)**, skyrmions become more pronounced, forming bubble-like magnetic textures. By 1.5 kOe **(g)**, the contrast vanishes, indicating that the system has reached a fully magnetized state with domains fully aligned along the applied field. The scale bar is 5 μm.

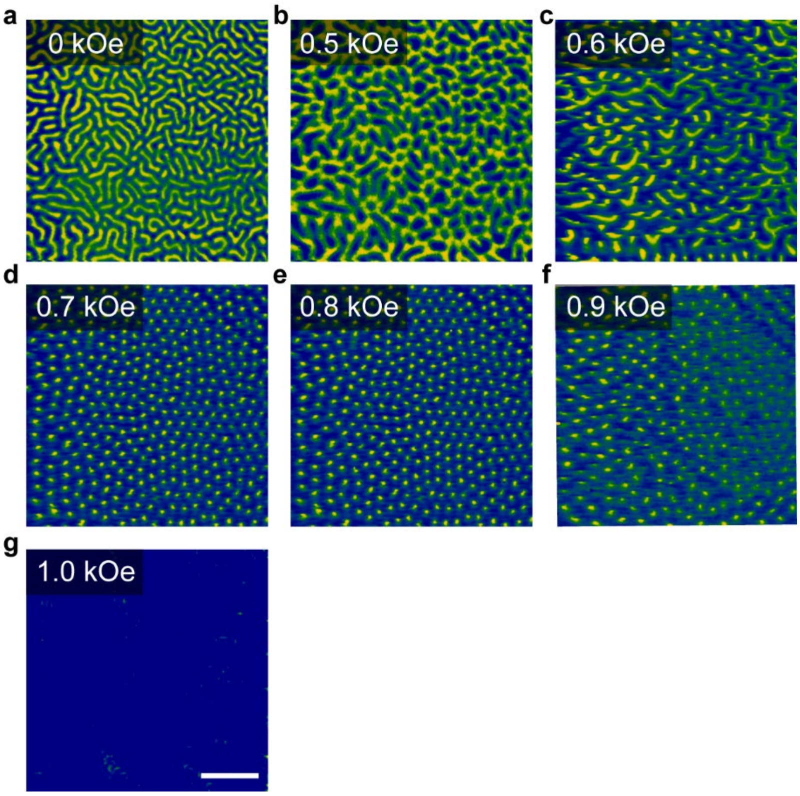

Figure S21 | Field-dependent magnetic force microscopy (MFM) imaging of annealed FGeT. (a–g) MFM images obtained under increasing external magnetic fields from 0 kOe to 1.0 kOe, illustrating the evolution of magnetic domain structures. At 0 kOe **(a)**, a well-defined labyrinth-like domain pattern is observed. As the field increases to 0.5 kOe **(b)** and 0.6 kOe **(c)**, domains begin to fragment, giving rise to skyrmion lattices. At 0.7 kOe **(d)** and 0.8 kOe **(e)**, a high-density skyrmion lattice is observed. At 0.9 kOe **(f)**, skyrmion lattice remains to be stable, but the contrast becomes vague. By 1.0 kOe **(g)**, the contrast vanishes, indicating that the system has reached a fully magnetized state with domains fully aligned along the applied field. The scale bar is 5 μm.

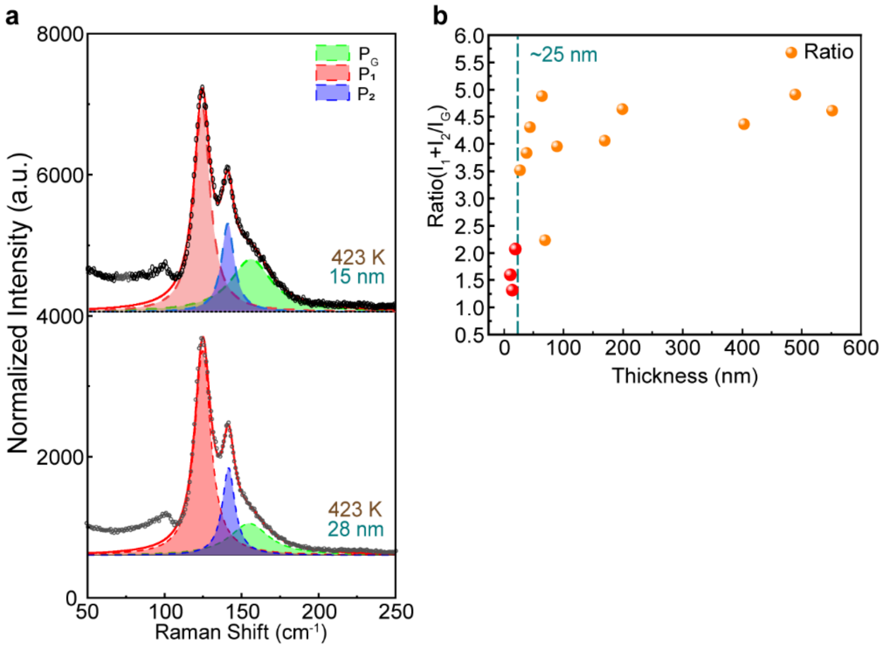

Figure S22 | Thickness and temperature dependence of Raman spectra in FGaT

(a) 15 nm (top) and 28 nm (bottom) FGaT at 423 K, illustrating the decomposition of spectral contributions. P_G is fitted Raman peak of FGaT, while P_1 and P_2 correspond to Raman peaks associated with $FeTe_2$. The presence of $FeTe_2$ peaks confirms the temperature-driven phase transformation. **(b)** Thickness dependence of the intensity ratio of (I_{FeTe_2}/I_{FGaT}) at 423K, revealing a critical thickness threshold of approximately 25 nm. Samples below 25 nm (red dots) exhibit a lower $FeTe_2$ intensity ratio, indicating reduced $FeTe_2$ formation, whereas samples exceeding 25 nm (orange dots) show a pronounced increase in $FeTe_2$ signal, suggesting enhanced precipitation over the thickness thershold.